Supplementary information

Resolving spectral overlap in ENDOR by chirp echo Fourier transform detection

Julian Stropp[a], Fabia Canonica[b], Nino Wili*[c], and Daniel Klose*[a]

[a] Department of Chemistry and Applied Bioscience, Institute for Molecular Physical Sciences, ETH Zürich, Vladimir-Prelog-Weg 2, 8093 Zürich, Switzerland
[b] Department of Biology, Institute of Molecular Biology and Biophysics, ETH Zürich, Otto-Stern-Weg 5, 8093 Zürich, Switzerland
[c] Interdisciplinary Nanoscience Center, Aarhus University, Gustav Wieds Vej 14, 8000 Aarhus C, Denmark

Contents

1 Phase cycling

All ENDOR experiments were performed with 4-step phase cycling. For Davies ENDOR the phase cycling was performed as $\pi_{\mathrm{MW,sel}}$ (0, 0, 0, 0) - π_{RF} (0, 0, 0, 0) - $\pi/2_{\mathrm{MW}}$ (0, 0, π, π) - π_{MW} (0, π, 0, π) - detection (0, 0, -1, -1). CHEESY ENDOR used the same phase cycling as Davies ENDOR with the last two MW pulses being chirped. The HYEND experiment used phase cycling of RF pulses: $\pi_{\mathrm{MW,sel}}$ (0, 0, 0, 0) - $\pi/2_{\mathrm{RF}}$ (0, 0, π, π) - π_{MW} (0, 0, 0, 0) - π_{MW} (0, 0, 0, 0) - $\pi/2_{\mathrm{RF}}$ (0, π, 0, π) - $\pi/2_{\mathrm{MW}}$ (0, 0, 0, 0) - π_{MW} (0, 0, 0, 0) - detection (0, -1, 0, -1). 2D Mims ENDOR spectra were obtained by $\pi/2_{\mathrm{MW}}$(0, π, 0, π) -π_{RF} (0, 0, 0, 0) - $\pi/2_{\mathrm{MW}}$ (0, 0, π, π) - $\pi/2_{\mathrm{MW}}$ (0, 0, 0, 0) - detection (0, -1, -1, 0).

2 Simulation algorithm

Simulations of CHEESY ENDOR spectra were performed with home-written MATLAB scripts, which are based on earlier work by Wili et al.[1] and use the EasySpin library.[2] The simulation algorithm - originally used to simulate EDNMR spectra[3] - was adapted to include excitation of NMR transitions by RF pulses.
The simulation is performed with the following steps:

1. Generation and diagonalization of the Hamiltonian for a certain orientation and a given spin system to obtain the energy levels, transition frequencies and their corresponding transition probabilities.

2. Selection of transitions that lie within the MW/RF pulse excitation bandwidths.

3. The population change is calculated from the hole weight HW for each EPR transition that is excited during the inversion pulse. The change depends on transition probability $P(\nu_{EPR})$, the offset of the transition frequency ν_{EPR} from the pulse frequency ν_{pulse} and the pulse bandwidth $\Delta\nu_{\mathrm{FWHM,pulse}}$.

$$HW = P(\nu_{EPR}) \cdot exp\left(-2\left(\frac{\nu_{EPR}-\nu_{\mathrm{pulse}}}{\Delta\nu_{\mathrm{FWHM,pulse}}}\right)^2\right) \tag{S1}$$

   The simulation code needs to be adapted, in case pulse types different from gauss pulses are used as inversion pulses.

4. The pump weight PW, which accounts for the population change during the RF pulse, is modeled with the Bloch equation. For a certain ENDOR transition ν_{ENDOR} the population change is determined by the ENDOR transition probability $P(\nu_{\mathrm{ENDOR}})$, the RF field strength ν_2 at the transition frequency frequency and the pulse duration T_{RF}.

$$PW = 1/2 - 1/2 \cdot \cos\left(2\pi\nu_2\sqrt{P(\nu_{\mathrm{ENDOR}})} \cdot T_{\mathrm{RF}}\right) \tag{S2}$$

   It is assumed that the RF field strength $\nu_{2,^1\mathrm{H}}$ is known from nutation experiments on protons and $\nu_2(\nu_{\mathrm{RF}})$ is extrapolated with a $1/\nu_{RF}$-dependence for all other pulse frequencies.

$$\nu_2(\nu_{\mathrm{RF}}) = \nu_{2,^1\mathrm{H}} \cdot \nu_{0,^1\mathrm{H}}/\nu_{\mathrm{RF}} \tag{S3}$$

   If the experimental frequency response function of ν_2 is known, it can be provided in the simulation script.

5. For each EPR transition and each connected ENDOR transition the difference in spin state populations before and after the RF pulse is calculated.

6. The signal for a given EPR transition detected with the chirp echo - arising from a specific initially excited EPR transition and a corresponding NMR transition - is calculated by weighting the population difference with the transition probability of the EPR transition, without explicitly considering the chirp echo detection efficiency. The CHEESY ENDOR spectrum is constructed by mapping the signal based on the corresponding EPR and ENDOR frequencies and summation over all excited NMR transitions and subsequently over all EPR transitions excited with the gauss inversion pulse.

7. Weighted summation over all excited orientations (powder average).

 DOI: 10.1039/D5CP03372A

3 Supplementary tables

3.1 BDPA spin Hamiltonian parameters

Table S1 Literature spin Hamiltonian parameters of BDPA[4,5] used in simulations, Euler angles of the interaction tensors are given with respect to the g-tensor = [2.00263, 2.00260, 2.00257].

Parameter	x/MHz	y/MHz	z/MHz	$\alpha/^\circ$	$\beta/^\circ$	$\gamma/^\circ$
A(^1H_a)	-7.7	-5.3	-2.2	0	0	0
A(^1H_b)	-7.7	-5.3	-2.2	0	67	90
A(^1H_c)	1.00	1.00	1.26	0	0	0

3.2 ScoI spin Hamiltonian parameters

Table S2 Spin Hamiltonian parameters of ScoI for simulations, Euler angles of the interaction tensors are given with respect to the g-tensor = $[2.0303 \pm 0.0005\ 2.0345 \pm 0.0005\ 2.1591]$. All parameters were determined previously using CW EPR[6], EDNMR, HYSCORE and ENDOR at X- and Q-band frequencies[7]. For Euler angles in brackets () no variation was required or performed to match experimental data, Euler angles with asterisk * are non-unique fitting solutions. For simulations of ^{15}N-labeled ScoI nitrogen couplings the respective values for ^{14}N were scaled by the gyromagnetic ratios.

Nucleus	A_x/MHz	A_y/MHz	A_z/MHz	$\alpha/^\circ$	$\beta/^\circ$	$\gamma/^\circ$
^{63}Cu	100 ± 4	124 ± 4	520.1	(0)	(0)	(0)
^{14}N	29 ± 2	38 ± 1	29 ± 1	46*	40*	16*
$^1H_\alpha$	20.5 ± 1.0	16.3 ± 1.0	16.0 ± 0.5	(0)	(0)	(0)
$^1H_\beta$	-1.5 ± 1.0	-10.0 ± 0.5	-1.5 ± 1.0	(0)	(0)	(0)
Nucleus	$eeQqh^{-1}$/MHz	η		$\alpha/^\circ$	$\beta/^\circ$	$\gamma/^\circ$
^{63}Cu	-28 ± 2	0.18 ± 0.18		(90)	(0)	(0)
^{14}N	2.5 ± 0.5	0.9 ± 0.1		47*	43*	17*

4 Supplementary figures

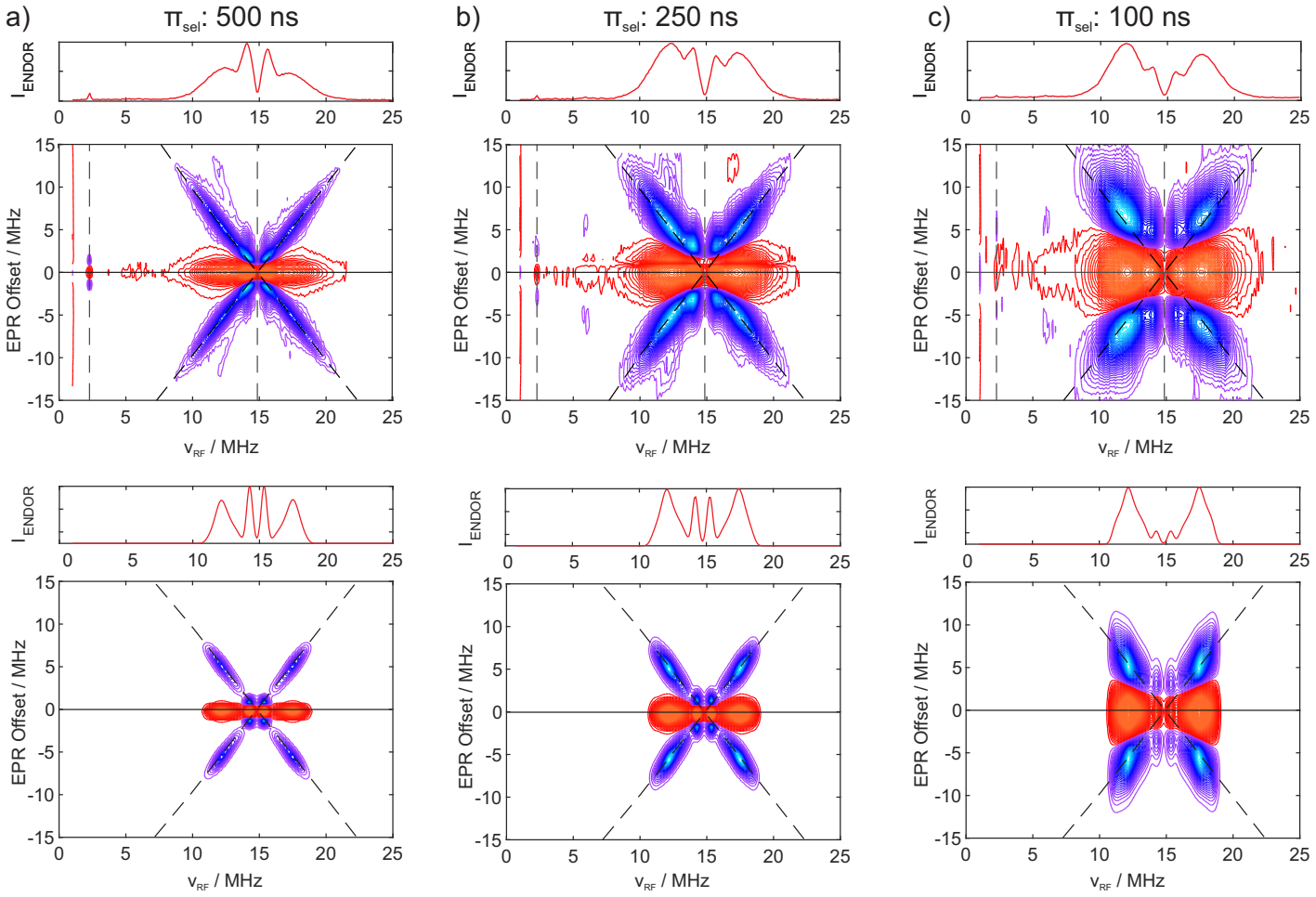

Fig. S1 X-band CHEESY ENDOR spectra of BDPA at 349 mT with different selective gauss inversion pulses π_{sel}: a) 500 ns b) 250 ns c) 100 ns. Experimental spectra (top) and simulated spectra (bottom) include a breakout spectrum of the integrated central hole (top). Simulation parameters can be found in Table S1.

 DOI: 10.1039/D5CP03372A

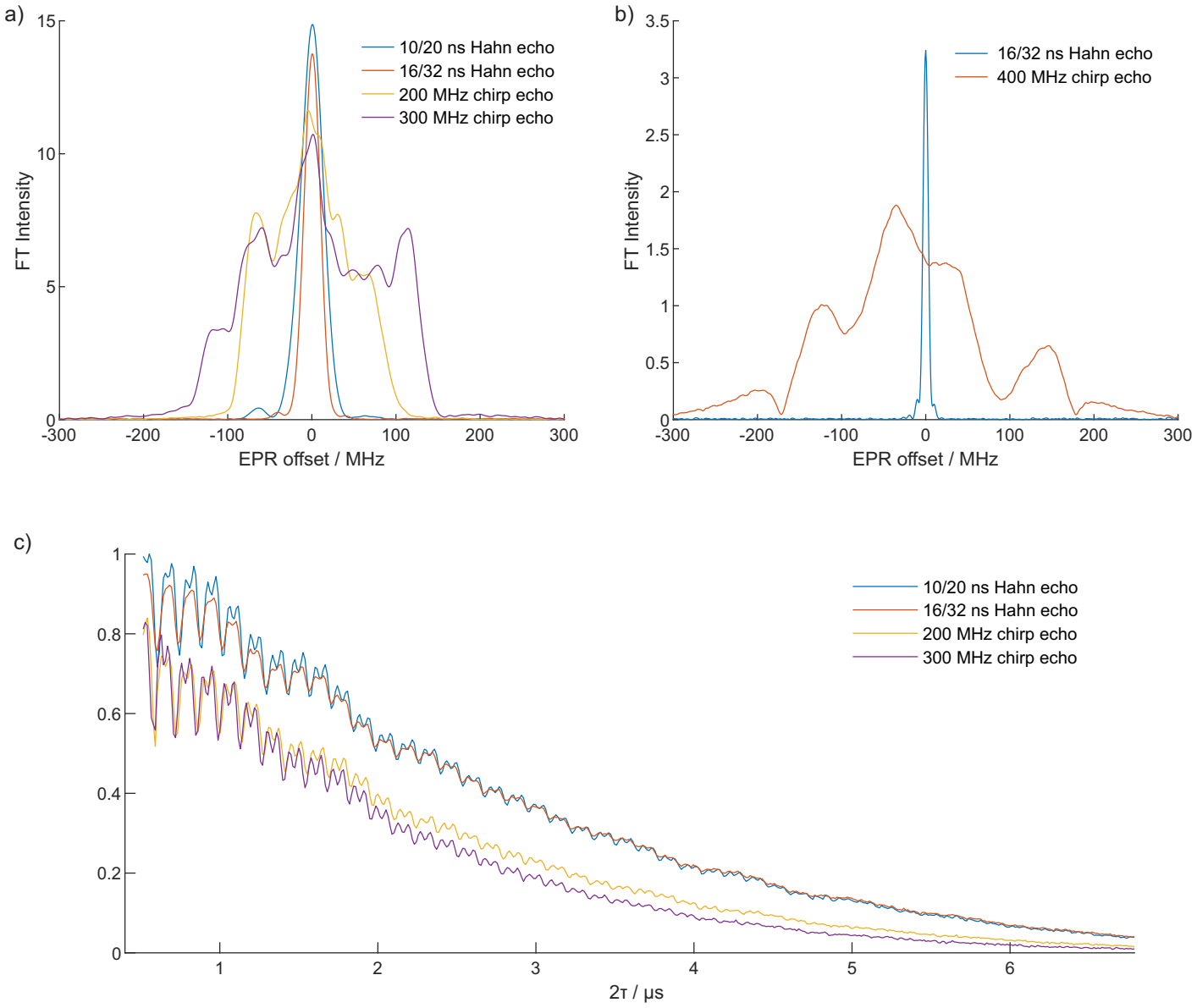

Fig. S2 Comparison of Hahn echo with chirp echo intensities after Fourier transformation on (^{15}N,^{63}Cu)-labeled ScoI·Cu^{2+} at 9.78 GHz (a) and 34.04 GHz (b). Parameters at 9.78 GHz: 340.0 mT, $\tau = 600$ ns, 200/100 ns chirp pulses; parameters at 34.04 GHz: 1192 mT. $\tau = 1000$ ns for the Hahn echo, $\tau = 900$ ns for the chirp pulses with 300/150 ns. The 2-pulse echo decay for the sequences shown in (a) is shown in (c).

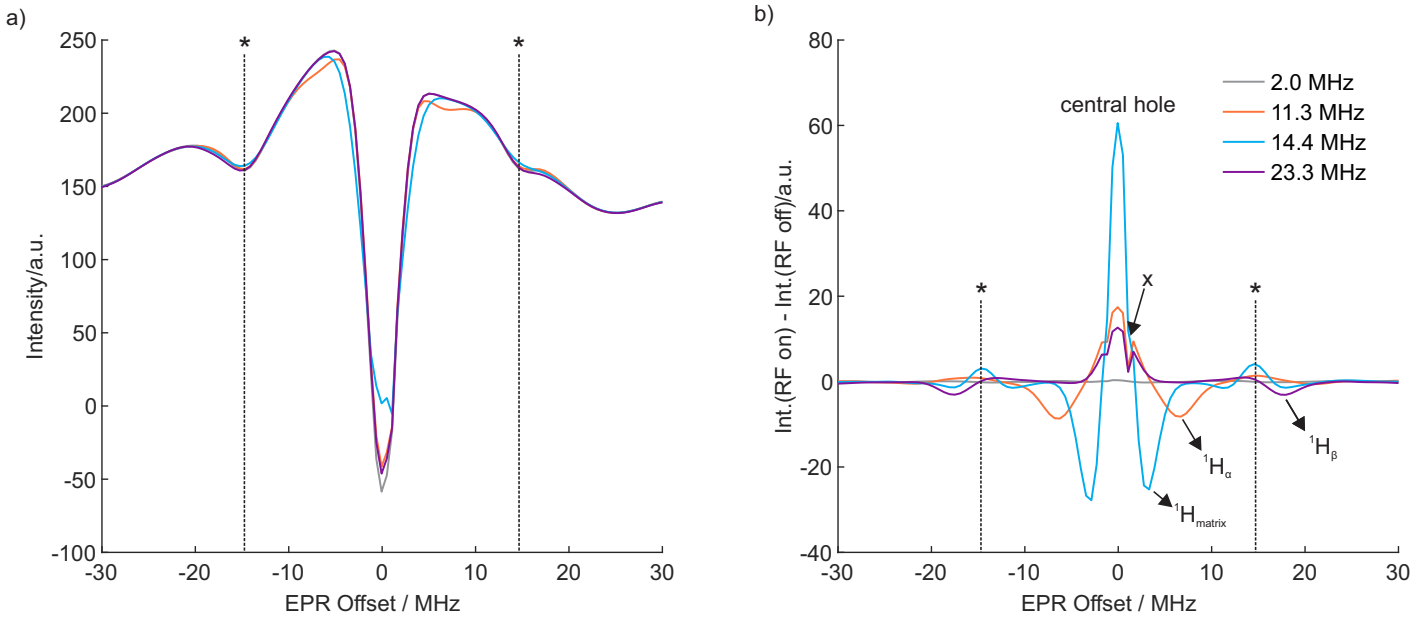

Fig. S3 Hole depth in CHEESY ENDOR. Vertical slices through the X-band CHEESY ENDOR spectrum of (^{15}N,^{63}Cu)-labeled ScoI·Cu^{2+} in Fig. 3a. Fourier-transformed chirp echo at four RF frequencies in a) and difference spectra as used for 2D CHEESY ENDOR in b). The arrows mark different sideholes due to hyperfine couplings as annotated. The asterisk (*) marks the sidehole position with positive peaks due to forbidden transitions. A slight distortion due to a phasing problem around the zero-crossing of the central hole intensity (left) is visible in the difference spectrum (marked with "x"). Depending on the RF pulse frequency negative sideholes appear at different EPR offsets (11.3 MHz for $^1H_\alpha$, 14.4 MHz for $^1H_{matrix}$ and 23.3 MHz for $^1H_\beta$). For off-resonance RF frequencies (2 MHz) the central hole is not shifted to sideholes and the diffeerence spectrum shows a flat line. Typically for ENDOR the central and side hole intensities are less than 1/10 of the echo intensity (except for the proton matrix peak (14.4 MHz)).

 DOI: 10.1039/D5CP03372A

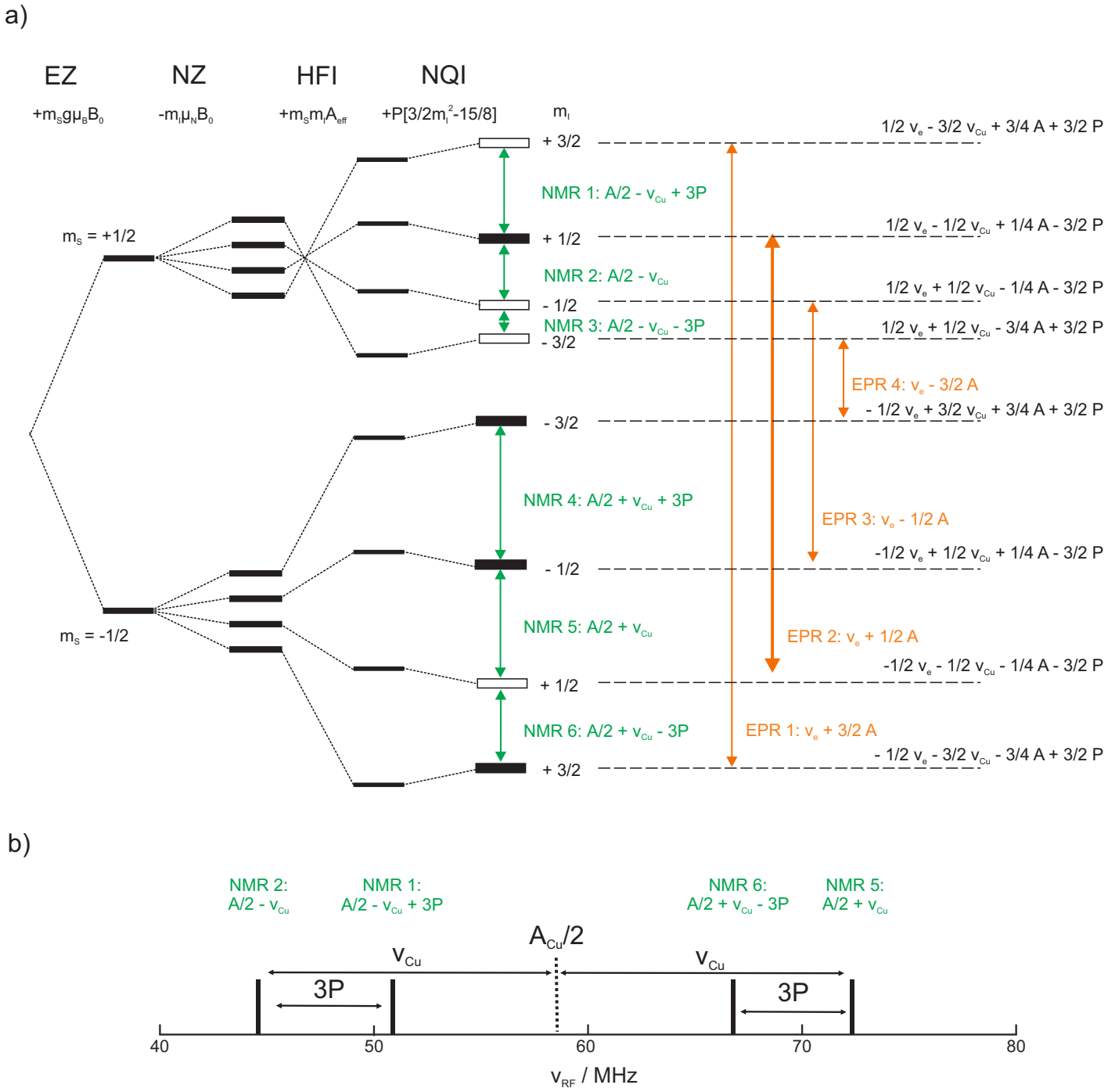

Fig. S4 a) Qualitative energy level diagram for a 2-spin system of an electron ($S = 1/2$) and a nucleus with $I = 3/2$ (e.g. ^{63}Cu). The scheme assumes that the nuclear quadrupole coupling is weak compared to nuclear Zeeman (NZ) and hyperfine (HFI) interactions and energies are given in the first order approximation. The boxes (filled/empty) indicate the populations after the initial MW inversion pulse in the CHEESY ENDOR experiment on ScoI in Fig. 3c ($B_{exp} = 1194$ mT). b) ENDOR stick spectrum corresponding to the energy level diagram and the populations illustrated in a).

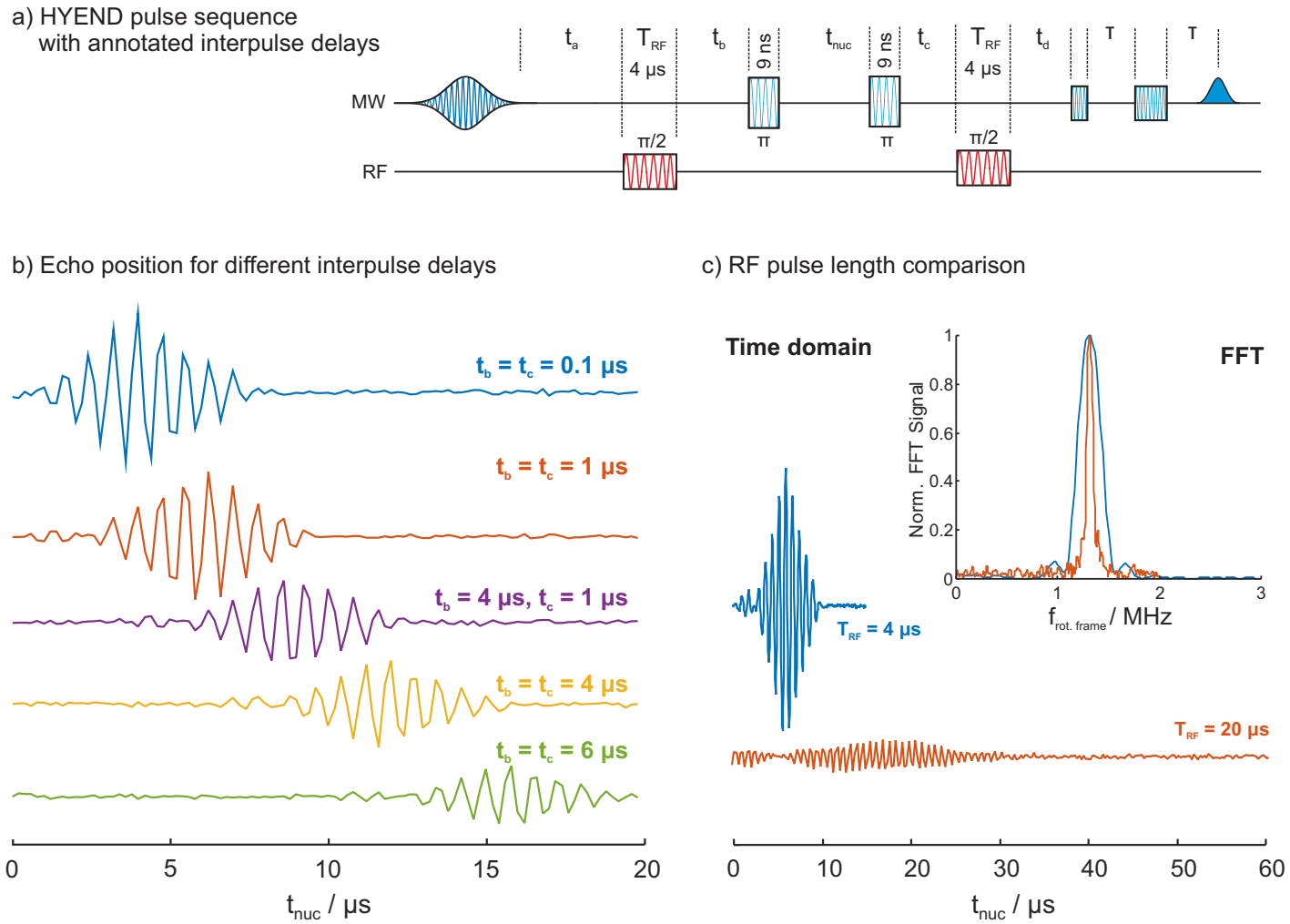

Fig. S5 Influence of interpulse delays and RF pulse length on the nuclear echo of BDPA in HYEND: a) Pulse sequence with annotated interpulse delays. b) Nuclear echoes measured for different interpulse delays t_b and t_c. The echo position is approximately at $t_{\mathrm{nuc}} = T_{\mathrm{RF}} + t_{\mathrm{b}} + t_{\mathrm{c}}$ with the RF pulse length T_{RF} of 4 µs. c) Comparison of the nuclear echo for different RF pulse powers/lengths with a frequency of 14.2 MHz detected in the rotating frame with the pulse frequency. The nuclear echo oscillates with the frequency of the connected NMR transition, which has a frequency difference of $A \approx 1.2$ MHz compared to the NMR transition excited with the RF pulse. A longer RF pulse with a smaller bandwidth leads to a longer decay of the nuclear echo and to a narrower peak in the frequency spectrum.

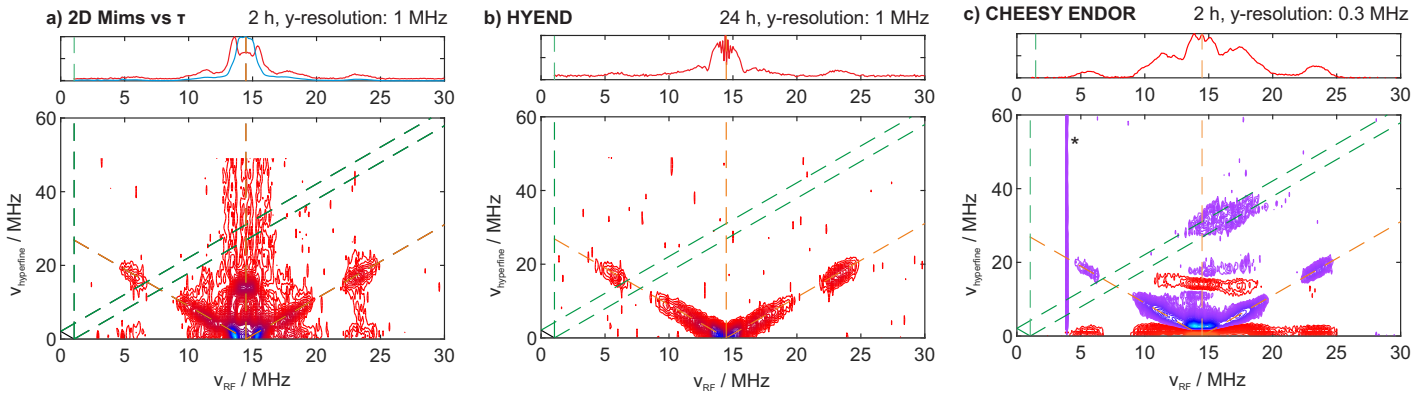

Fig. S6 Comparison of CHEESY ENDOR to established 2D ENDOR experiments with a hyperfine dimension for (^{14}N, ^{63}Cu)-labeled ScoI·Cu^{2+} in X band and 340 mT: a) 2D Mims ENDOR with 60 τ-values starting at 160 ns and increments of 10 ns. The 1D trace shows the sum of the Mims ENDOR spectra (blue) and the sum of the 2D FT spectrum (red). b) HYEND with a 250 ns gauss inversion pulse and t_{nuc} with 60 steps of 10 ns. The 1D trace shows the sum of the 2D FT spectrum. c) 2D CHEESY ENDOR spectrum with 250 ns gauss inversion pulse and the integrated central hole intensity (top). The bottom half ($\nu_{\mathrm{hyperfine}} < 0$ MHz) was added onto the top half of the 2D spectrum. Asterisk (*) marks an artifact. Larmor frequencies and sidehole ridges for ^{1}H and ^{14}N are marked with dashed lines in orange and green, respectively. For each experiment the measurement time and resolution of the hyperfine axis are given in the top right corner.

 DOI: 10.1039/D5CP03372A

References

1 N. Wili, S. Richert, B. Limburg, S. J. Clarke, H. L. Anderson, C. R. Timmel and G. Jeschke, *Physical Chemistry Chemical Physics*, 2019, **21**, 11676–11688.

2 S. Stoll and A. Schweiger, *Journal of Magnetic Resonance*, 2006, **178**, 42–55.

3 N. Cox, A. Nalepa, W. Lubitz and A. Savitsky, *Journal of Magnetic Resonance*, 2017, **280**, 63–78.

4 R. Rizzato, I. Kaminker, S. Vega and M. Bennati, *Molecular Physics*, 2013, **111**, 2809–2823.

5 M. Bennati, C. Farrar, J. Bryant, S. Inati, V. Weis, G. Gerfen, P. Riggs-Gelasco, J. Stubbe and R. Griffin, *Journal of Magnetic Resonance*, 1999, **138**, 232–243.

6 F. Canonica, D. Klose, R. Ledermann, M. M. Sauer, H. K. Abicht, N. Quade, A. D. Gossert, S. Chesnov, H.-M. Fischer, G. Jeschke, H. Hennecke and R. Glockshuber, *Science Advances*, 2019, **5**, eaaw8478.

7 J. Stropp, *MSc thesis*, ETH Zurich, 2021.